Characterizing how order gives way to spatiotemporal chaos in two-dimensional pattern-forming systems

Eduardo A. Droguett-Mora [1,*] Cristina Masoller [2] and Marcel G. Clerc [1]

[1]*Departamento de Física and Millennium Institute for Research in Optics, Facultad de Ciencias Físicas y Matemáticas, Universidad de Chile, Casilla 487-3, Santiago, Chile*

[2]*Department of Physics, Universitat Politecnica de Catalunya, 08222 Terrassa, Barcelona, Spain*

(Received 15 December 2025; accepted 4 March 2026; published 23 March 2026)

Systems with energy injection and dissipation are characterized by self-organization through spontaneous breaking of translational symmetry, giving rise to the formation of patterns. Depending on the energy injection, patterns can be regular in space and stationary, or exhibit irregular spatial distributions and complex temporal dynamics. The emergence of complexity in two-dimensional patterns is not yet fully understood nor characterized. Based on a liquid crystal light valve with optical feedback, we characterize experimentally the formation of a pattern in the presence of noise and the route to the spatiotemporal complexity. A universal model of pattern formation, valid close to nascent bistability and spatial bifurcation, is also numerically simulated and studied. In the experimental and in the simulated data, the spatiotemporal complexity is characterized via several complexity measures that provide complementary information. We find that, when varying the control parameter, from the homogeneous state, a stationary pattern emerges, which then becomes chaotic, with characteristic temporal dynamics and spatial irregularities. These transitions were correctly identified by a clustering algorithm. Our results pave the way for future studies of other pattern-forming complex systems.

DOI: 10.1103/rdhb-x2gv

I. INTRODUCTION

Macroscopic systems under a permanent injection and dissipation of energy can exhibit periodic spatial structures that result from the self-organization of their constituents [1–4]. These spatial structures, usually called *patterns*, have an intrinsic wavelength and arise from a homogeneous steady state through a spatial breaking symmetry instability [2]. Patterns can be found in various nonlinear out-of-equilibrium systems [5], such as magnetic fluids [6], gas [7], semiconductor laser [8], and liquid crystals [9], among others (see Refs. [1–5] and references therein). As one increases a bifurcation parameter, these stationary patterns are formed, presenting in some cases complex spatial distributions [2–5,10–12]. Stationary patterns have been extensively studied, and the mechanisms of pattern formation are well understood [1–5]. When the bifurcation parameter is further increased, these stationary patterns acquire complex spatiotemporal dynamics. Dynamical patterns have been observed, for example, in chemical reactions [13], fluidized granular matter [14], electroconvection [15], and nonlinear optics [16], to mention a few. The understanding of how pattern-forming systems acquire spatiotemporal complexity has been studied theoretically in one dimension [17], but in two dimensions is still incomplete.

Theoretically, the spatial continuous instability usually leads to a pattern with an amplitude that increases as the square root of the bifurcation parameter. Due to the macroscopic nature of the experiments, there are inherent fluctuations of the physical system under study, i.e., noise. One can consider the effect of noise by adding a stochastic term in the partial differential equation that describes the system under study [18]. The stochastic term modifies the bifurcation, leading to a different scaling of the pattern amplitude with respect to the bifurcation parameter [19].

To understand how the two-dimensional pattern acquires spatiotemporal complex dynamics, a characterization of the complexity is needed. One first statistical approach to characterize how the temporal complexity emerges is the recognition of characteristic decays in the *spectral density*. Power law decays for a decade or a few decades of frequencies in the power spectral density have been observed for different quantities in systems that exhibit turbulentlike behaviors. These decays appear due to the participation of different temporal modes and the absence of structures at different scales [16,20–27]. To understand the dynamical nature of the complexity in the system, one can compute the largest Lyapunov exponent (LLE) of the solutions [28], providing information about the exponential sensitivity to the initial conditions. The computation of the largest Lyapunov exponent for an experimental system is computationally expensive; therefore, one wants to find other complexity parameters to characterize the spatiotemporal dynamics further. The *permutation entropy* (PE) is a complexity parameter that is shown to behave similarly

*Contact author: eduardo.droguett@ug.uchile.cl

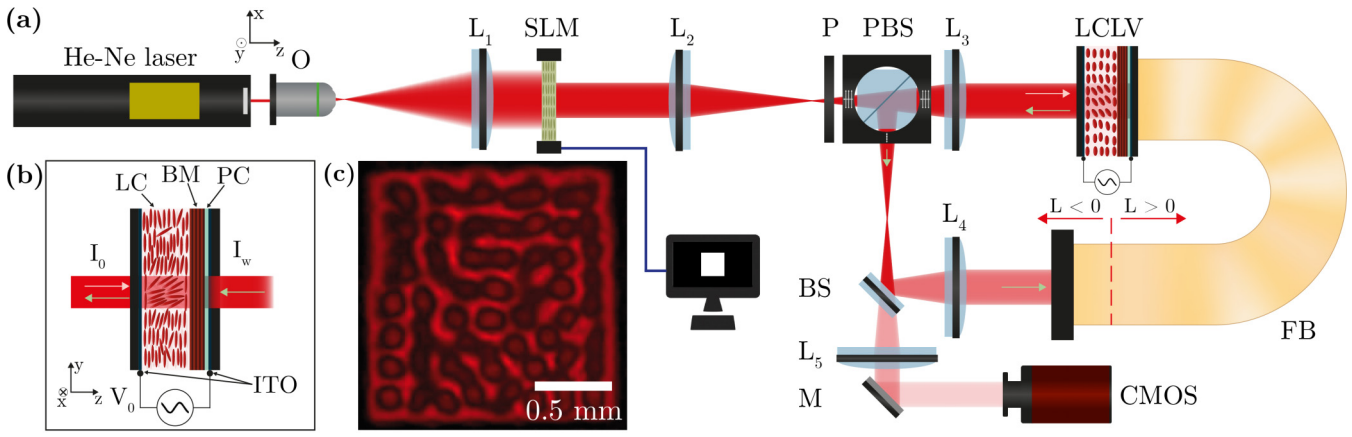

FIG. 1. LCLV with optical feedback. (a) Schematic representation of the experimental setup. He-Ne accounts for a helium-neon laser light source, O is an optical objective with magnification $\times 20$, L_i stands for lens, SLM is a spatial light modulator, P is a $\lambda/2$ polarizer, PBS corresponds to a polarizer beam splitter, BS is a beam splitter, FB is a high-resolution optical fiber bundle, M stands for mirror, CMOS accounts for a complementary metal-oxide-semiconductor camera, and L is the diffraction length. (b) Schematic representation of the LCLV. LC accounts for the liquid crystal layer, BM is a Bragg mirror, PC is a photoconductive layer, ITO are transparent indium tin oxide electrodes, V_0 is the driving voltage, I_0 is the laser intensity, and I_w is the writing intensity after passing through the LCLV. (c) Snapshot of a recorded liquid crystal pattern.

to the largest Lyapunov exponent, but it is characterized by its simplicity, extremely fast calculation, and noise robustness [29,30]. By studying the relative values in subsequent instants of the system's temporal evolution, the permutation entropy gives information about the presence of characteristic dynamics. The permutation entropy has been used as a complexity measure in various systems, such as liquid crystals [31], vegetation landscapes [32], semiconductor lasers [33–37], among others. This method can be extended to study the spatial organization of the system by analyzing the relative values of subsequent points in the extended system [38], giving the *spatial permutation entropy* (SPE). Finally, as these two entropies only give information about the relative values of subsequent points, one can also compute the entropy of the distribution of data values in each frame, referred in the following as *frame entropy* (FE), which quantifies the level of heterogeneity of the data values in each frame.

Here, based on an optical experiment, a liquid crystal light valve (LCLV) with optical feedback (see Fig. 1), we study and characterize the route to complexity. This system has been widely studied and characterized [22,39–43], due to its simplicity in controlling and exploring different variational and nonvariational phenomena, together with its spatial and temporal scales that make measurements and characterization more accessible. By analyzing the light transmitted through the optical valve, the spatial instability that initially forms the static pattern is studied, giving the bifurcation point and the noise level intensity associated with the experimental system. We then characterize the spatiotemporal complexity exhibited by the patterns formed in this optical system by using the power spectral density, the largest Lyapunov exponent, and spatiotemporal permutation entropies. The light intensity field bifurcates in a way that, first, from the homogeneous state, a stationary pattern is formed, and then acquires spatiotemporal complex dynamics. To contrast the experimental characterization, we numerically integrated a universal pattern-forming model, the nonvariational Turing-Swift-Hohenberg equation, that can be derived from the phenomenological model of the LCLV [44]. The initial homogeneous state exhibits nonchaotic dynamics with flat temporal spectral densities, a largest Lyapunov exponent close to 0, and high spatiotemporal permutation entropies, due to the dominance of noise in the observed dynamics. When the pattern is formed, the spatial permutation entropy decreases, indicating an increase of spatial order in the system. The frame entropy increases, showing that the intensity values become more heterogeneous. Once the temporal dynamics appear, a characteristic power law decay in the power spectral density can be observed, and the dynamics becomes chaotic. The spatiotemporal permutation entropies are increased due to the chaotic dynamics. The numerical simulations of the nonvariational Turing-Swift-Hohenberg are in fair agreement with the experimental observations. This characterization helps elucidate the underlying dynamics that give rise to spatiotemporal complexity in two-dimensional pattern-forming systems.

II. EXPERIMENTAL SETUP

To study and characterize the route to complexity in two-dimensional patterns, we use a simple physical system that exhibits pattern formation with nonvariational behaviors, the liquid crystal light valve with optical feedback [22,39–43]. Figure 1(a) shows a schematic representation of the LCLV with optical feedback setup. The liquid crystal light valve is composed of a nematic liquid crystal LC-654 (NIOPIK) with a dielectric anisotropy constant $\epsilon_a = 10.7\epsilon_0$ (with ϵ_0 being the dielectric constant of the vacuum) placed between two glass layers that are separated by a distance $d = 15$ μm. Transparent indium tin oxide electrodes and a photoconductive layer are deposited on the glass to maintain the liquid crystal to a driven oscillatory voltage $V_0 = 7.45$ mV rms with frequency $f_0 = 1.0$ kHz. A dielectric Bragg mirror optimized for reflectivity at 632.8 nm light is placed at the back of the liquid crystal cell. The liquid crystal has planar anchoring, that is, the molecules

on the cell wall are attached so that the director vector $\vec{n}$ is parallel to this wall. The director $\vec{n}(\vec{r}, t)$ accounts for the average orientation of the molecules at position $\vec{r}$ and instant t. Figure 1(b) shows a schematic representation of the LCLV.

The valve is optically forced with a He-Ne laser with wavelength $\lambda_0 = 632.8$ nm at intensity $I_0 = 0.1$ mW/cm^2. The LCLV is placed in a $4f$ optical configuration ($f = 25$ cm). The optical feedback loop is closed with an optical fiber bundle (FB) that injects the light into the photoconductive layer, applying an additional voltage to the liquid crystal material depending on the local light intensity I_w. This feedback loop is designed so that light simultaneously presents polarization interference, induced by the polarizing beam splitter, and free diffraction caused by the displacement of the FB entrance by a distance L from the original $4f$ configuration [45]. This distance is controlled by a servo motor (Thorlabs LTS300/M-300 mm Translation Stage with Stepper Motor). A spatial light modulator (SLM, LC 2012 spatial light modulator Holoeye, transmission) is considered to carry out the square boundary conditions. This SLM consists of a twisted nematic liquid crystal display, which generates a simple phase modulation and a coupled polarization effect that results likewise in an amplitude modulation. The experiment is monitored and recorded by a complementary metal-oxide-semiconductor (CMOS) camera.

The path and optical elements are placed such that the surface of the LCLV is observed by the CMOS and retroinjected by the FB, so that the intensity I_w can be related to the average molecule angle $\theta(x, y, t)$ by [45]

$$I_w(\theta, L) = \frac{I_0}{4}|e^{-i(L/2k)\nabla^2}(1 - e^{-i\beta\cos^2\theta})|^2, \qquad (1)$$

where $\{x, y\}$ are the transversal spatial coordinates, and $\beta\cos^2\theta$ is the overall phase shift experienced by the light traveling forth and back through the liquid crystal layer. $\beta = 2kd\Delta n$, where $k = 2\pi/\lambda_0$ is the optical wave number and $\Delta n = 0.2$ is the difference between the extraordinary ($\parallel$ to $\vec{n}$) and ordinary ($\perp$ to $\vec{n}$) index of refraction of the liquid crystal. For the values considered in our experiment, $\beta \approx 54$. All experiments were conducted at a working temperature $T \approx 25^\circ$ C. The full theoretical description of the experimental system can be found in Appendix A

Data acquisition

To characterize the route to complexity of the two-dimensional optical patterns, we have studied the solution exhibited by the system when using an intensity mask of zero-level intensity everywhere except for a central square part with length $a_0 = 1.8$ mm with 46 different diffraction lengths $0 < -L < 10$ cm. For $L > 0$, the system presents other phenomenology such as localized structures that are not the scope of this study [41]. When changing the diffraction length, we waited a time $t \sim 5$ min for the system to reach a qualitative equilibrium, and then the subsequent 30 000 frames were recorded at a rate of 45 FPS (around 11 min), and then used to perform the data analysis. The original 8-bit videos were a sequence of square frames with 452×452 pixels each, covering a region of 1.95×1.95 mm^2. To ensure that the results were not affected by boundary artifacts, the analysis was performed on a central square of 272×272 pixels.

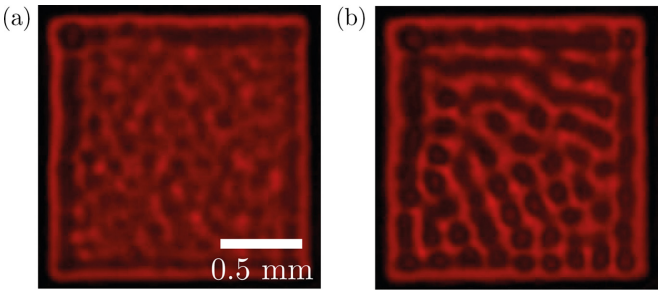

FIG. 2. Image of the liquid crystal light valve recorded with CMOS camera (a) below and (b) above the spatial bifurcation. Diffraction length: (a) $-L = 1$ cm and (b) $-L = 3$ cm.

III. RESULTS

A. Pattern formation in the presence of noise

The studied system exhibits pattern formation from a uniform state. When $-L \ll 1$ cm, the system presents the homogeneous solution. Then, by increasing the diffraction length, a spatial instability occurs, and the solution changes to a static pattern as a consequence of the spontaneous spatial symmetry breaking. Theoretically and close to the bifurcation, the deterministic case leads to an amplitude that increases with the square root of the bifurcation parameter [2]. Namely, this spatial instability corresponds to a supercritical transition. Figures 2(a) and 2(b) show the experimental state below and above the spatial bifurcation. It is noteworthy that even when the system is below the spatial bifurcation, it exhibits patternlike structures or precursor phenomena [46], and the state is not entirely homogeneous. These patternlike structures are called *pattern precursors* and are caused by the presence of inherent fluctuations (noise) in the system [46]. Noise excites all spatial modes permanently, but the slowest mode leads the dynamics [19]. Above the spatial bifurcation, a pattern with small fluctuations is formed. It is noteworthy that nonvariational effects do not cause these fluctuations; These fluctuations arise due to experimental noise and are, in fact, much smaller than the ones that are produced by the nonvariational dynamics.

Figure 3 shows the experimental bifurcation diagram of the pattern amplitude $|A|$ as a function of the diffraction length L

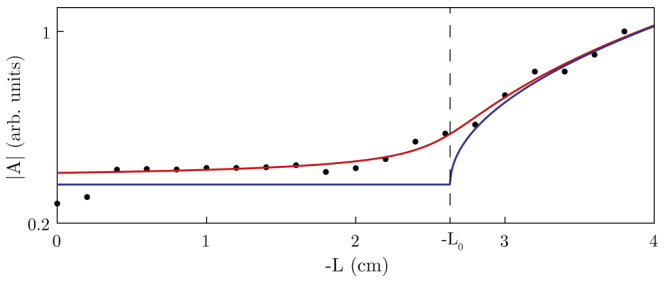

FIG. 3. Pattern amplitude $|A|$ as a function of the diffraction length L. The black points correspond to the experimental data. The red (blue) curve is the stochastic (deterministic) supercritical bifurcation fit. $-L_0 = 2.6322$ cm is the critical point of spatial bifurcation obtained using the stochastic supercritical fit.

with the fitted stochastic supercritical curve [46]:

$$|A| = \sqrt{\frac{-\alpha(L-L_0)+\alpha\sqrt{(L-L_0)^2+2\xi/\alpha^2}}{2}} + |A_0|, \quad (2)$$

and the deterministic supercritical curve,

$$|A| = \sqrt{-\alpha(L-L_0)} + |A_0|. \quad (3)$$

For these disordered patterns, with a typical length but oriented in all directions, a powdered ring is expected [12]. The pattern amplitude was obtained by means of the fast Fourier transform (FFT). The FFT was averaged in time, and then an angular average was obtained. The maximum of this curve was considered the pattern amplitude. For representation purposes, all the maxima were normalized by the last amplitude. The derivation of the theoretical curves is explained in Appendix A.

The obtained parameters are $\alpha = 0.3193$ cm^{-1}, $-L_0 = 2.6322$ cm, $\sqrt{\xi}/\alpha = 0.6614$ cm, and $|A_0| = 0.3612$. Note that L_0 gives the theoretical spatial bifurcation point, and $\sqrt{\xi}/\alpha$ accounts for the noise level intensity with respect to the diffraction length. In the next section, we characterize the spatiotemporal complexity exhibited by the two-dimensional patterns.

B. Complexity characterization

In the experimental system under study, when one increases $-L$ beyond the spatial bifurcation, the dynamics become nonvariational due to the nonlocal spatial dependence of I_w. This causes the pattern to acquire permanent dynamics that exhibit spatiotemporal complexity.

To further understand the route to complexity in two-dimensional patterns, the nonvariational Turing-Swift-Hohenberg equation was also integrated. This model reads

$$\partial_t u = \eta + \mu u - u^3 + \nu\nabla^2 u - \nabla^4 u + \kappa u\nabla^2 u + c(\nabla u)^2. \quad (4)$$

The parameters used are $\eta = 0.09$, $\mu = 0.4$, $\nu = -0.1$, $c = 15$, and different nonlinear diffusion parameters $2.5 < -\kappa < 3.34$. A slight multiplicative noise was also added. For the lower bound of $-\kappa$, the observed solution was homogeneous. In a similar manner to the experimental observations, when increasing $-b$, a spatial instability occurs, and the solution changes to a static pattern. Finally, for the upper bound, one can observe a pattern with permanent and complex spatiotemporal dynamics.

The recorded videos and the numerical simulations are analyzed in the following subsections in terms of different complexity parameters.

All of the computed curves presented in the next subsections were fed into a clustering algorithm. More information about the clustering process can be found in Appendix C. The three clusters, labeled as blue, green, and orange, can be physically interpreted as homogeneous, static pattern, and dynamic pattern solutions, respectively. Figure 4 shows snapshots of characteristic solutions of each cluster, as well as Videos 1 and 2 in the Supplemental Material [47].

1. Spectral characterization

When studying the complexity of a solution, an important tool is the temporal *power spectral density* ($\mathcal{PSD}$) (see Appendix D 1 for details [48]). At each point in space where we measure the intensity $I(r, t)$, we can calculate the spectral density by means of the following expression $\mathcal{PSD} \equiv \int_\Omega dr \int dt e^{i\nu t}|I(r,t)|^2/\Omega\sqrt{2\pi}$, where Ω is the spatial area of the region under study. The permanent energy injection can produce secondary instabilities that generate oscillations and complex spatiotemporal behaviors, leading to a wide range of temporal frequencies participating in the permanent dynamics [42,49–51], and characteristic decays in the power spectral density.

Figures 5(a) and 5(b) show the power spectral density for three different experimental and numerical solutions, characteristic of each cluster. In both cases, for a small bifurcation parameter, the power spectral density is dominated

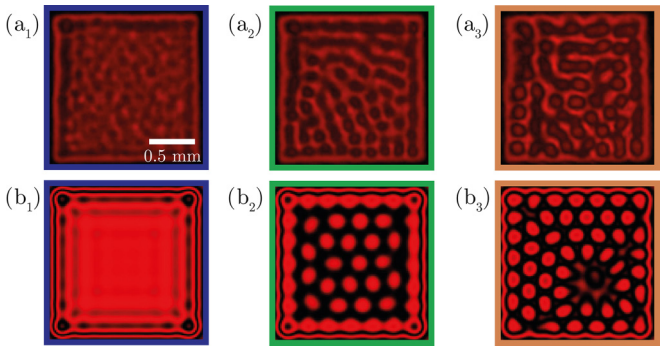

FIG. 4. Characteristic behaviors of the LCLV with optical feedback. Blue-green-orange frame accounts for the homogeneous, static pattern, and dynamic pattern behaviors. (a) Snapshots of the recorded experimental data at (a$_1$) $-L = 1$ cm, (a$_2$) $-L = 3$ cm, and (a$_3$) $-L = 6$ cm, respectively. (b) Snapshots of the integrated numerical data at (b$_1$) $-\kappa = 2.50$, (b$_2$) $-\kappa = 2.80$, and (b$_3$) $-\kappa = 3.14$, respectively.

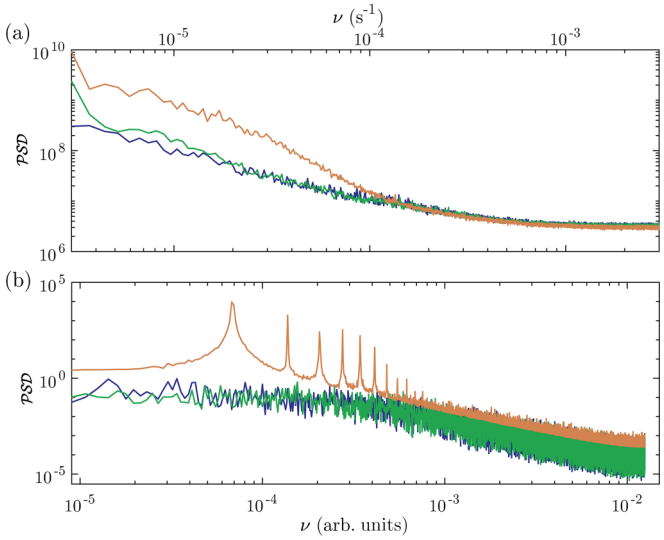

FIG. 5. $\mathcal{PSD}$ as a function of the frequency ν. The blue-green-orange colors represent the different clusters obtained using the k-means algorithm with three clusters. These clusters can be interpreted as homogeneous, static patterns, and dynamic pattern regions. (a) Experimental data at $-L = 1$, 3, and 6 cm. (b) Numerical data at $-\kappa = 2.50$, 2.80, and 3.14. The spectra were computed for each pixel and then averaged.

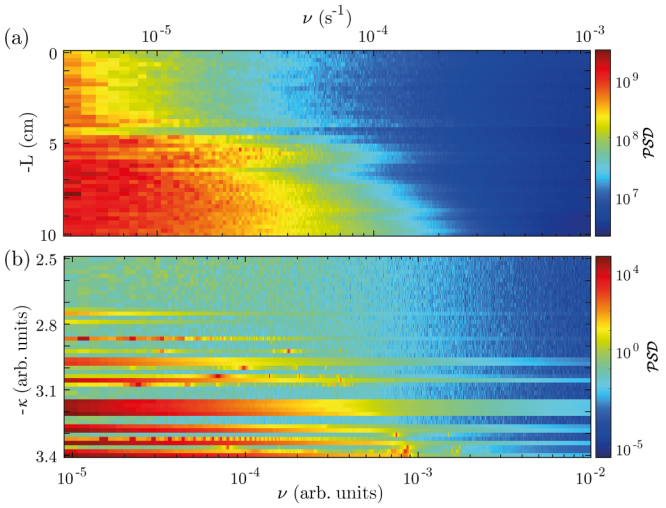

FIG. 6. $\mathcal{PSD}$ for varying diffraction length L and nonlinear diffusion b. (a) Experimental data. (b) Numerical data.

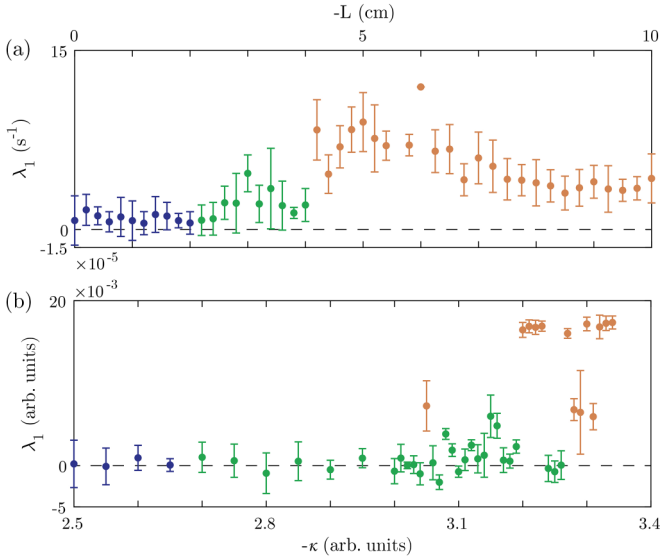

FIG. 7. Largest Lyapunov exponent λ_1 for varying diffraction length L and nonlinear diffusion κ. (a) Experimental data. (b) Numerical data. The blue-green-orange colors represent the different clusters obtained using the k-means algorithm with three clusters. These clusters can be interpreted as homogeneous, static patterns, and dynamic pattern regions. The plotted points correspond to the spatial average, and the error bars account for the standard deviation of the data.

by noise (small decays and flat curves). Still, when the bifurcation parameter is increased, the curves exhibit characteristic decays, and, in the numerical case, peaks for specific frequencies appear. For a more objective classification of experimental and numerical observations, we used the k-means algorithm with three clusters, each corresponding to a homogeneous state, a static pattern, and a chaotic pattern. In Fig. 5, the blue-green-orange colors represent the different clusters. The power spectral density as a function of the diffraction length is shown in Fig. 6. Then, as the free diffraction increases, the complexity of the system increases. We observe a similar behavior for the nonvariational parameter that accounts for the nonlinear diffusion in Eq. (4).

2. Largest Lyapunov exponent

The characterization of the complexity can be done by means of analyzing the sensitivity to the initial conditions that the Lyapunov exponents characterize. There are as many exponents as the dimension of the system under study. Still, in practice (due to the exponential nature of the dynamics), one can only access experimentally to the LLE λ_1. This is done by means of the recognition of similar frames in a temporal evolution, and using them as similar initial conditions [52] as explained in Appendix D 2 [43]. By itself, the LLE gives information about the rate of exponential growth or shrinking of an initially infinitesimal perturbation, and therefore, the sensitivity to initial conditions. Depending on the sign of λ_1, the infinitesimal perturbation exhibits an exponential growth ($\lambda_1 > 0$) or shrinking ($\lambda_1 < 0$). When $\lambda_1 \sim 0$, one can observe dynamical behaviors that correspond to an equilibrium with invariant directions, such as periodic or quasiperiodic solutions and nonchaotic attractors [53].

Figure 7(a) shows the experimental LLE. For a small diffraction length, the system has an LLE close to 0. When increasing this parameter, the system becomes chaotic. Based on the k-means algorithm, we identified three clusters corresponding to a homogeneous state, a static pattern, and a chaotic one. Figure 7(b) shows the numerical LLE for varying the nonlinear diffusion parameter κ. For small nonlinear diffusion, the system also has an LLE close to 0. When increasing this parameter, the system becomes intermittently chaotic.

3. Permutation entropy

The search and study for similar initial conditions is computationally expensive, and the LLE only gives information about the sensitivity to initial conditions; therefore, one wants to find other complexity parameters to further characterize the observed phenomena. The PE is a complexity parameter characterized by its simplicity, swift calculation, and noise robustness [29]. To compute the PE, symbols of a certain length are defined as permutation of the relative values at subsequent points in a time series. The PE is calculated as explained in Appendix D 3 [29]. Figures 8(a) and 8(b) show the computed permutation entropy for the experimental and numerical data, respectively. In both cases, the system initially has the maximum entropy, but as the dynamics appear, this entropy is then lowered. For small values of the control parameter, the system has no dynamics, i.e., is stationary. When the system is stationary, the presence of stochastic fluctuations in both the experimental and numerical data leads to a random temporal evolution (all symbols are equiprobable), therefore, a maximal permutation entropy. Once the system acquires characteristic dynamics that are more relevant than stochastic fluctuations (see Videos 1 and 2 in the Supplemental Material [47]), some symbols become more probable; therefore, the permutation entropy decreases (for the experimental data, this occurs for $L \approx -4$ cm, while for the numerical data, for $\kappa \approx 3$). Finally, as the system acquires its maximal temporal complexity, the permutation entropy increases again. This indicates that the

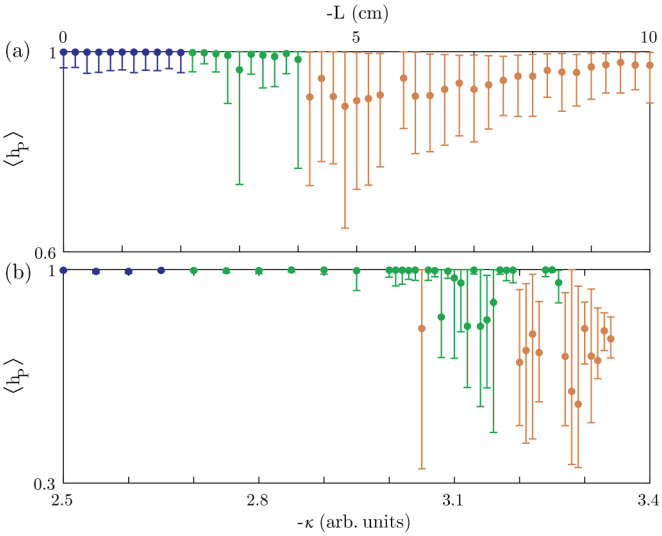

FIG. 8. Permutation entropy $\langle h_{SP} \rangle$ for varying diffraction length L and nonlinear diffusion κ. (a) Permutation entropy as a function of diffraction length L for experimental data. (b) Permutation entropy as a function of nonlinear diffusion parameter κ for numerical data. The blue-green-orange colors represent the different clusters obtained using the k-means algorithm with three clusters. These clusters can be interpreted as homogeneous, static patterns, and dynamic pattern regions. The plotted points correspond to the spatial average, and the error bars account for the minimum and maximum values obtained.

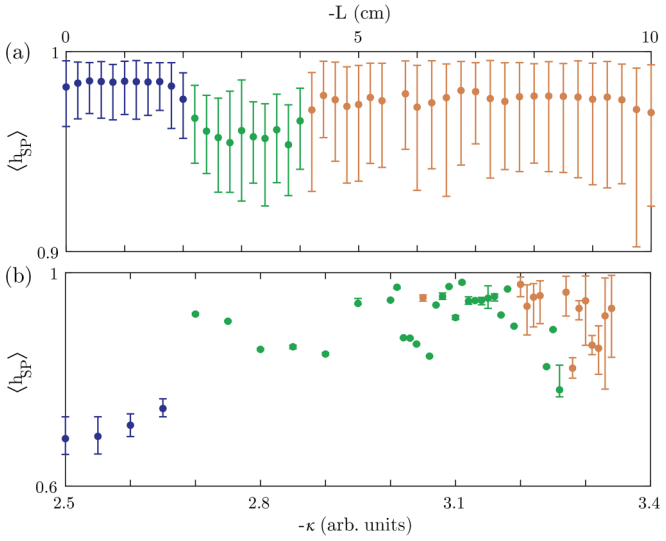

FIG. 9. Spatial permutation entropy $\langle h_{SP} \rangle$ for varying diffraction length L and nonlinear diffusion b. (a) Experimental data. (b) Numerical data. The blue-green-orange colors represent the different clusters obtained using the k-means algorithm with three clusters. These clusters can be interpreted as homogeneous, static patterns, and dynamic pattern regions. The plotted points correspond to the spatial average, and the error bars account for the minimum and maximum values obtained.

fully developed complexity of the system leads to effective stochasticity.

4. Spatial permutation entropy

The PE computation can now be performed in the spatial dimension, obtaining the SPE. The SPE is calculated as explained in Appendix D 4 [29]. This can give information about the spatial distribution of the system. Figure 9(a) shows the SPE for the experimental data. Initially, the SPE is high due to the system spatial variations being mainly caused by noise. When the pattern is formed, the SPE is lowered. Finally, as the pattern becomes dynamic, the SPE is again increased due to the spatial irregularities introduced by the dynamics. Analogously, Fig. 9(b) exhibits the SPE for the numerical data. Initially, the SPE is low, probably due to the presence of a pattern precursor. As the nonlinear diffusion is increased, the emergence of pattern defects increases the SPE. Finally, in a manner similar to the experimental data, due to the dynamics of the pattern, the SPE reaches its maximum, i.e., there is an irregular spatial distribution.

5. Frame entropy

Another statistical quantity that can shed light on the observed complexity is the *frame entropy*. This entropy can complement the previously computed entropies by providing information about the distribution of intensities within the system, beyond just their relative value distribution. The FE is calculated as explained in Appendix D 5. Figures 10(a) and 10(b) show the frame entropy for the experimental and numerical data, respectively. In both cases, for a small value of the control parameter, the frame entropy is minimum, due to the system being in a homogeneous state. As the bifurcation parameter increases, spatial variations appear, thus more intensities are reached, increasing the frame entropy. The frame entropy saturates due to the saturation of the pattern amplitude.

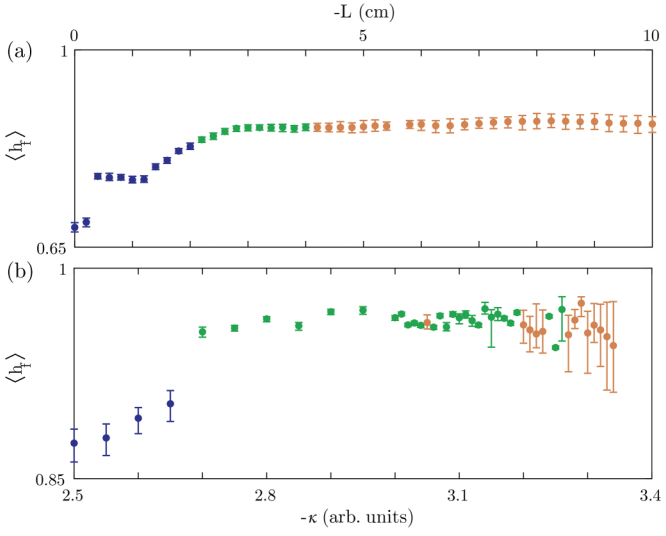

FIG. 10. Frame entropy $\langle h_f \rangle$ as a function of diffraction length L [panel (a)] and nonlinear diffusion κ [panel (b)]. The blue-green-orange colors represent the different clusters obtained using the k-means algorithm with three clusters. These clusters can be interpreted as homogeneous, static patterns, and dynamic pattern regions. The plotted points correspond to the spatial average, and the error bars account for the minimum and maximum values obtained.

IV. DISCUSSIONS

The onset of the spatial instability leading to pattern formation in our experimental system is characterized by the emergence of pattern precursors. It has been shown that, in the theoretical transition from order to spatiotemporal chaos in an extended system, pattern precursors of fully developed spatiotemporal chaos may appear before the transition to permanent spatiotemporal chaos due to the embedded chaotic saddle of the system [54]. In our experimental system, however, pattern precursors were only identified in the stationary spatial bifurcation. We therefore have attributed this modification of the bifurcation to the noise caused by different stochastic fluctuations, such as thermal and electric. The emergence of pattern precursors may thus result from a combination of these mechanisms, due to the possibility of the system exhibiting a *noise-induced chaotic attractor* or *stochastic chaotic saddles*, where the coexistence of a chaotic saddle and a periodic attractor results in a chaotic attractor under noise [55].

Due to the spatiotemporal nature of the system, a single indicator is insufficient for comprehending the observed phenomena. The permutation entropy indicates the emergence of dynamics in the system. The nature of these dynamics can be studied with the largest Lyapunov exponent, which characterizes the difficulty in making predictions. The route from order to spatiotemporal complexity should involve hyperchaos [54]; therefore, the computation of the full Lyapunov spectrum would be ideal. In practice, however, due to the exponential sensitivity governed by the Lyapunov exponents, only the largest Lyapunov exponent can be reliably accessed experimentally [43]. This proved sufficient to characterize the transition from nonchaotic dynamics to chaotic dynamics when complemented with the other complexity metrics. Projecting the various unstable directions and characterizing the different Lyapunov exponents is, experimentally, a monumental task. This represents a significant gap between experimental and theoretical possibilities for characterizing complex spacetime dynamics, requiring the use of more advanced analysis tools. The spatial permutation entropy indicates transitions in the spatial distribution of the system. The transition between a homogeneous state, a pattern, and a disordered pattern can only be pictured by this indicator. The first transition is complemented by the frame entropy, indicating that more intensity states are reached as one increases the control parameter, increasing the frame entropy.

To further understand the pattern formation from the homogeneous state, a model that considers the stochastic aspect of the system was taken into account. This allowed us to obtain the point of spatial bifurcation of the system and its noise.

The numerical data obtained from the universal model capture several qualitative features observed experimentally, although some differences remain. The numerical simulations accurately capture the presence of three regimes (the homogeneous state, the stationary pattern, and the dynamic pattern), and also exhibit the same key features of the fully developed complexity, i.e., characteristic chaotic dynamics with irregular spatial distributions.

The main discrepancies between the experiments and simulations lie in the dynamic pattern regime. Specifically, the intermittent nature of the complexity and the emergence of characteristic frequencies are observed in the numerical simulations. We think that the presence of noise, inhomogeneities, and/or misalignments within the experimental system contributes to the complexity and defect creation, thereby precluding the possibility of stationary patterns appearing when the diffraction length is sufficiently high. This can also be attributed to the local approximation of the model. We think that a higher noise intensity, or the inclusion of inhomogeneities in the parameters in the simulations of model [Eq. (4)], could lead to a better agreement with the experimental results.

V. CONCLUSION

By using an experimental system based on a liquid crystal light valve with optical feedback, we have characterized the emergence of two-dimensional spatiotemporal complex optical patterns. By inserting free diffraction, the system presents a spatial instability that led to a stationary pattern. When further increasing the diffraction length, the system became nonvariational, inducing nontransient complex spatiotemporal dynamics.

The first bifurcation was characterized using a model that considers the stochastic aspect of the system induced by the macroscopic nature of the system, allowing for the determination of the point of spatial bifurcation and the noise associated.

The emergence of the spatiotemporal complexity is characterized by characteristic power law decays in the power spectral density, and chaotic dynamics associated with the increase of the largest Lyapunov exponent. Furthermore, this complexity is characterized by a lowered permutation entropy, indicating that characteristic dynamics rule the system, and a high spatial permutation entropy, indicating that the spatial distribution of the system is irregular. The entropy of the frames exhibited an initial increase due to the pattern forming.

The regions of homogeneous, static patterns, and spatiotemporal complex patterns were correctly differentiated by the clustering algorithm, demonstrating its usefulness for distinguishing transitions when provided with the appropriate metrics that characterize the system.

These features of the complexity in two-dimensional optical patterns were also obtained by integrating a universal model of pattern formation derived from the phenomenological model of the experimental system. This indicates that these findings are intrinsic to two-dimensional patterns and contribute to a deeper understanding of the mechanisms driving spatiotemporal complexity in two-dimensional patterns. Therefore, these results should be observed in other physical systems that present spatiotemporal complex patterns, such as fluid convection, active matter, driven granular materials, fiber and semiconductor lasers, nonlinear optical systems, and ecological and biological systems, to mention a few. While meticulous studies investigate primary pattern instabilities in these systems, research on the complexity of these patterns away from primary bifurcations is limited.

ACKNOWLEDGMENTS

E.A.D.-M. and M.G.C. acknowledge financial support from ANID-Millennium Science Initiative Program No.

ICN17_012 (MIRO). C.M. acknowledges partial support from ICREA ACADEMIA and Agencia Estatal de Investigación (Grant No. PID2024-160573NB-I00).

DATA AVAILABILITY

The data that support the findings of this article are not publicly available. The data are available from the authors upon reasonable request.

APPENDIX A: THEORETICAL DESCRIPTION OF THE EXPERIMENT

In the absence of light on the photoconductor, the effective electric field E_{eff} applied to the liquid crystal layer is $E_{\text{eff}}(I_w = 0) = \Gamma V_0/d$, where $\Gamma < 1$ is a transfer factor that depends on the electrical characteristics of the photoconductor, dielectric mirror, and the liquid crystal layer (impedances). As long as the light intensity is sufficiently small (on the order of a few mW/cm^{-2}), the response of the photoconductor can be fitted by a linear function. Under this approximation, the total effective electric field applied to the liquid crystal film can be expressed as $E_{\text{eff}} = \Gamma V_0/d + \alpha I_w$, where α is a phenomenological dimensional parameter that can be quantitatively evaluated by fitting the open-loop response of the LCLV [41]. $\theta = 0$ is the initial unperturbed planar alignment, whereas $\theta = \pi/2$ is the homeotropic alignment corresponding to the saturation of the molecular reorientation. The liquid crystal dynamics is described by a local relaxation equation of the form [39]

$$\tau \partial_t \theta = l^2 \nabla^2 \theta - \theta + \frac{\pi}{2}\left(1 - \sqrt{\frac{\Gamma V_{\text{FT}}}{\Gamma V_0 + \alpha d I_w(\theta, L)}}\right), \quad \text{(A1)}$$

with $V_{\text{eff}} \equiv \Gamma V_0 + \alpha d I_w(\theta, L) > V_{\text{FT}}$, where $V_{\text{FT}} = 3.2\ V_{\text{rms}}$ [41,56] is the Fréedericksz transition threshold voltage and l is the electric coherence length. It is important to remark that the above model has been deduced by fitting the experimental data measured for the open-loop response of the LCLV [41].

The homogeneous equilibrium solutions are $\theta_0 = 0$ and $\theta_0 = \pi/2(1 - \sqrt{V_{\text{FT}}/V_{\text{eff}}})$ when $V_{\text{eff}} \leqslant V_{\text{FT}}$ and $V_{\text{eff}} > V_{\text{FT}}$, respectively. Above the Fréedericksz transition, if we neglect the spatial couplings and search for equilibrium solutions, we find a closed expression for θ_0:

$$\theta_0 = \frac{\pi}{2}\left(1 - \sqrt{\frac{\Gamma V_{\text{FT}}}{\Gamma V_0 + 2\alpha d I_0 \sin^2[\beta \cos^2 \theta_0/2]}}\right). \quad \text{(A2)}$$

The above expression for θ_0 presents several branches of bistability. Let us now consider the spatial effects due to the elasticity of the liquid crystal and to the light diffraction induced by moving the L parameter in the optical feedback. The system also exhibits a spatial instability. The point of parameter space that shows simultaneously a nascent bistability and a spatial bifurcation, a Lifshitz point [2], gives rise to a critical point of codimension three. Close to this point, we can expand $\theta(x, y, t) = \theta_0 + u(x, y, t) + \cdots$, and after straightforward calculations, one can derive Eq. (4) [44].

The relationship between the parameters of this equation and the physical parameters of the model [Eq. (A1)] is explained in detail in Ref. [44]. The parameter μ accounts for the bifurcation parameter, η describes the size of the bistability region, and ν is the diffusion parameter ($\nu > 0$) or antidiffusion ($\nu < 0$); this parameter controls the spatial instability at long wavelengths. The term $\nabla^4 u$ describes a hyperdiffusion that accounts for the short-distance repulsive interaction. On the other hand, the terms proportional to κ and c are, respectively, the nonlinear diffusion and drift. Note that both of these parameters are proportional to the diffraction length. Notice that when both of these parameters are 0, the Turing-Swift-Hohenberg equation is recovered, which is variational, leading to a static pattern as a stable solution. To derive the previous Eq. (4), the following scaling is considered $\partial_t \sim \mu^{1/2}$, $\nabla \sim \mu^{1/4}$, $u \sim \mu$, $\eta \sim \mu^{3/2}$, $\nu \sim \mu^{1/2}$, $\kappa \sim c \sim \mathcal{O}(1)$, and $\mu \ll 1$.

To understand how noise affects the pattern formation, one can study the Turing-Swift-Hohenberg model [Eq. (4)] in the variational case ($\kappa = c = 0$) with $\eta = 0$ and add a stochastic term $\sqrt{\xi}\zeta(x, y, t)$ that accounts for the noise effect, where ξ is a parameter that accounts for the noise intensity level, and $\zeta(x, y, t)$ is a Gaussian white noise. The Gaussian white noise has the following properties:

$$\begin{aligned} &\langle \zeta(x, y, t) \rangle = 0, \\ &\langle \zeta(x, y, t), \zeta(x', y', t') \rangle = \delta(x - x')\delta(y - y')\delta(t - t'), \end{aligned} \quad \text{(A3)}$$

where the symbol $\langle \cdot \rangle$ accounts for the average over the noise realizations.

Close to the spatial instability, one can introduce the following ansatz:

$$u = u_0 + A(X, Y, T)e^{i\vec{k}\cdot\vec{r}} + \bar{A}(X, Y, T)e^{-i\vec{k}\cdot\vec{r}}, \quad \text{(A4)}$$

with $(X, Y) = \sqrt{\mu}(x, y)$ and $T = \mu t$. A is a complex variable that accounts for the pattern amplitude. It has been shown [19] that the pattern amplitude in the presence of noise is given by

$$|A| = \sqrt{\frac{\mu + \sqrt{\mu^2 + 2\xi}}{2}}. \quad \text{(A5)}$$

Note that for the deterministic case ($\xi = 0$), one recovers the universal square-root scaling of a supercritical bifurcation.

APPENDIX B: NUMERICAL SIMULATIONS

To solve the model [Eq. (4)], we discretize the space by using a pseudospectral method with a spatial step of $\Delta x = 0.4$ in a square grid of 100×100 with periodic boundary conditions. The equation is numerically integrated in time with the Runge-Kutta four time integrator with temporal step $\Delta t = 0.0001$. Random initial conditions were used, and the system was evolved until a qualitative equilibrium was reached (5000 000 time steps). Then, 3500 000 time steps were recorded, saving every 250 frames to perform the reported analysis.

To emulate Neumann boundary conditions, a linear ramp was used, i.e., near the boundaries, μ is decreased to $\mu \ll 0$. Note that when $\mu \ll 0$, the stable solution of Eq. (4) is $u(x, y, t) = 0$. To avoid boundary artifacts, a central square region of 60 pixels in length was used to perform the analysis.

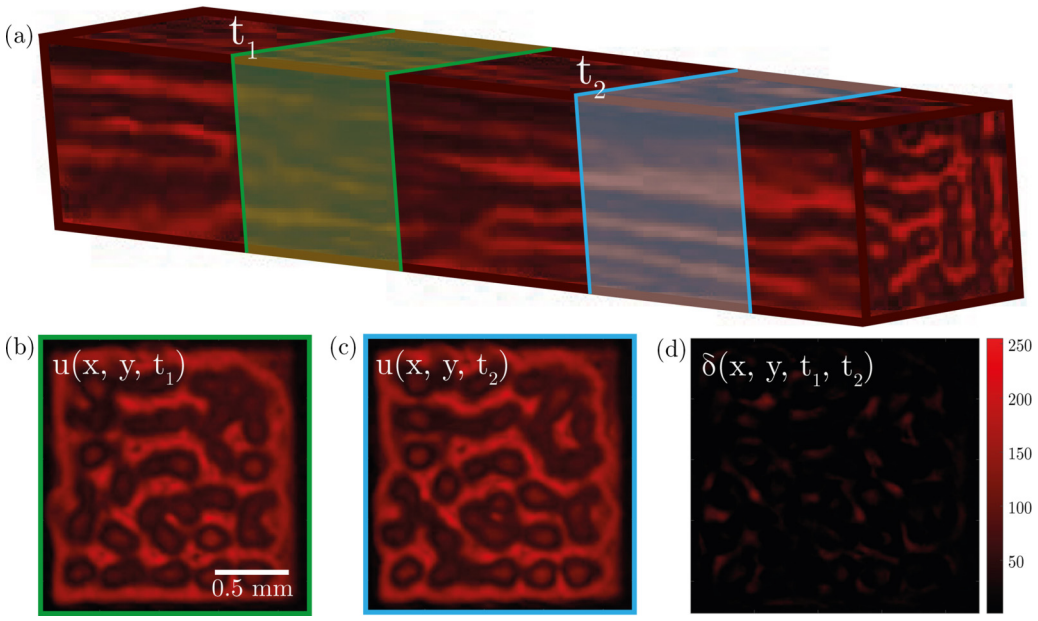

FIG. 11. Similar frames detected in the temporal evolution. (a) Spatiotemporal diagram of the recorded solutions. t_1 and t_2 are the frames where the system exhibited a similar state. Snapshots of the solutions in panel (b) t_1 and panel (c) t_2. (d) The difference field $\delta(x, y, t_1, t_2)$ of the solutions.

APPENDIX C: DATA CLUSTERING

To clusterize the data, we used the k-means algorithm with 100 replicates (i.e., 100 different random initializations to ensure robustness). Three clusters were chosen; the city-block distance was used for the experimental data, and the square Euclidean distance was used for the numerical data, as these options maximized the silhouette factor ($\sim$0.6 in both the experimental and numerical data), which quantifies the clusters' compactness and separation. The largest Lyapunov exponent, permutation entropy, spatial permutation entropy, and frame entropy were all used to find the three clusters.

APPENDIX D: COMPLEXITY METRICS

1. Temporal power spectral density

The recorded videos and numerical solutions are noted as $u(x, y, t)$, where (x, y) accounts for the spatial pixel location, and t is the frame. The temporal power spectral density is computed as [48]

$$\mathcal{PSD} = \frac{1}{N^2}\sum_{x=1}^{N}\sum_{y=1}^{N}|\mathcal{F}[u^2]|^2(x, y, \nu), \tag{D1}$$

where $\mathcal{F}$ is the Fourier transform in the time dimension and ν is the frequency.

2. Largest Lyapunov exponent

Because of the impossibility of preparing experimentally the system with infinitesimally separated initial conditions, to compute the experimental largest Lyapunov exponent, two similar frames are searched along the recorded evolution. Only frames separated by $\Delta t > \Delta t_0$ are taken into account. Based on the difference field $\delta(\vec{r}, t_1, t_2) = |u(\vec{r}, t_1) - u(\vec{r}, t_2)|$ between the frames, two indicators were used to quantize the similarities between the frames. The *maximal difference* (MD) allows us to detect pronounced differences in the frame pair. It is defined as

$$\delta_M(t_1, t_2) = \max_{\{x,y\}} \delta(x, y, t_1, t_2). \tag{D2}$$

The *global mean difference* (GMD) allows us to quantify the global similarity between the frames. It reads

$$\delta_G(t_1, t_2) = \frac{1}{N^2}\sum_{x=1}^{N}\sum_{y=1}^{N}\delta(x, y, t_1, t_2), \tag{D3}$$

where N is the length in pixels for each direction. By using these indicators, an algorithm that searches similar frames in a recorded video can be constructed. Figure 11 shows two similar frames detected in the temporal evolution by this algorithm, and their respective difference field $\delta(\vec{r}, t_1, t_2)$

Once a set of similar frame pairs $\{(t_1, t_2)\}$ is found, the global difference is tracked in time, and the largest Lyapunov exponent is defined by [43]

$$\lambda_1 = \lim_{t\to\infty}\lim_{\delta_G(t_1,t_2)\to 0}\frac{1}{t}\ln\left[\frac{\delta_G(t_1 + t, t_2 + t)}{\delta_G(t_1, t_2)}\right]. \tag{D4}$$

For each experimental point, from 1 to 12 initial conditions were found for $\Delta t_0 \approx 45$ s, with a global mean difference less than 0.01, and a maximal difference near 0.19 (both of these quantities were normalized to the maximum possible difference, i.e., 255 bits). The maximum GMD and MD were 0.02 and 0.50, respectively.

To compute the largest Lyapunov exponent of the numerical simulations, we took the evolved solutions in the qualitative equilibria and added random noise on the order of 10^{-3} to the final state. We then evolved the solutions with and without the noise for 3500 000 time steps. Finally, we

computed the LLE as Eq. (D4) indicates. This procedure was performed four times.

3. Permutation entropy

To compute the permutation entropy, symbols of a certain length n are defined as the permutation of the relative values in i subsequent points (separated by a characteristic time τ) in a time series. These symbols are then identified through the time series under study, and a frequentist probability of each symbol is defined. The normalized permutation entropy is then defined as [29]

$$H_n = -\frac{1}{\ln[n!]} \sum_m p(m) \ln[p(m)], \tag{D5}$$

where $p(m)$ is the probability for a symbol m of length n. In our study, $n = 4$ was used as the symbol length. Other symbol lengths $n > 2$ yielded similar curves.

Note that $0 \leqslant H_n \leqslant 1$, where the lower bound is obtained for an increasing or decreasing time series and the upper bound for a completely random system, where all the symbols appear with the same probability. Therefore, when the system presents some sort of dynamics, one can expect to obtain a permutation entropy $H_n < 1$. It has been shown that the permutation entropy behaves similarly to the LLE, and is particularly useful in the presence of dynamical or observational noise [29]. When plotting the $H_n(\tau)$, a local minimum is observed. The characteristic time τ for the computation of the PE is where the minimum occurs.

To avoid encountering equal values, an infinitesimal noise was added to the data. The reported permutation entropy is the average for every pixel, i.e.,

$$\langle h_P \rangle = \frac{1}{N^2} \sum_{x=1}^{N} \sum_{y=1}^{N} H_4(x, y), \tag{D6}$$

where N is the length in pixels for each direction.

4. Spatial permutation entropy

The symbols are now identified for each frame, and then the average is obtained for the total evolution. This can give information on the spatial distribution of the solution; a low (high) SPE indicates that the system is ordered (disordered) in space.

Because of the two-dimensional nature of the observed phenomena, the symbols can be defined in different shapes. The normalized spatial permutation entropy is then defined as

$$H'_n = -\frac{1}{\ln[n!]} \sum_m p(m) \ln[p(m)], \tag{D7}$$

where $p(m)$ is the probability for a symbol m of length n. In our study, the characteristic distance used between the points was the pattern wavelength. $n = 4$ was used as the symbol length, and because of the square boundary conditions of the system, the chosen symbol shape was a square (2×2 square). Other shapes yielded mostly constant curves, giving no information about the transitions in the spatial complexity of the solution.

The reported spatial permutation entropy is the average for every frame, i.e.,

$$\langle h_{\mathrm{SP}} \rangle = \frac{1}{M} \sum_{z=1}^{M} H'_4(z), \tag{D8}$$

where M is the number of frames.

5. Frame entropy

To compute this quantity, the intensities for each frame are divided into 256 bins (the natural division for the 8-bit images obtained), and then the frequency of occurrence for each intensity is computed. The normalized frame entropy is then defined

$$H = -\frac{1}{\ln[256]} \sum_{i=0}^{255} p(I_i) \ln[p(I_i)], \tag{D9}$$

where I_i are the different recorded light intensities in 8-bit.

Note that $0 \leqslant h_{\mathrm{frame}} \leqslant 1$, where the lower bound is obtained for a homogeneous state and the upper bound for a completely random state, where all the intensities appear with the same probability. The reported frame entropy is the average for every frame, i.e.,

$$\langle h_f \rangle = \frac{1}{M} \sum_{z=1}^{M} H(z), \tag{D10}$$

where, again, M is the number of frames.

[1] G. Nicolis, *Self-Organization in Non-Equilibrium Systems, from Dissipative Structures to Order through Fluctuations* (Wiley, New York, 1977).

[2] M. C. Cross and P. C. Hohenberg, Pattern formation outside of equilibrium, Rev. Mod. Phys. **65**, 851 (1993).

[3] L. M. Pismen, *Patterns and Interfaces in Dissipative Dynamics* (Springer, Berlin, 2006), Vol. 706.

[4] M. Cross and H. Greenside, *Pattern Formation and Dynamics in Nonequilibrium Systems* (Cambridge University Press, Cambridge, 2009).

[5] M. Tlidi, M. G. Clerc, and K. Panajotov, Dissipative structures in matter out of equilibrium: From chemistry, photonics and biology, the legacy of Ilya Prigogine (part 1), Philos. Trans. R. Soc. A **376**, 20180114 (2018).

[6] R. E. Rosensweig, M. Zahn, and R. Shumovich, Labyrinthine instability in magnetic and dielectric fluids, J. Magn. Magn. Mater. **39**, 127 (1983).

[7] D. Dangoisse, D. Hennequin, C. Lepers, E. Louvergneaux, and P. Glorieux, Two-dimensional optical lattices in a CO_2 laser, Phys. Rev. A **46**, 5955 (1992).

[8] A. Bartolo, N. Vigne, M. Marconi, G. Beaudoin, K. Pantzas, I. Sagnes, G. Huyet, F. Maucher, S. Gurevich, J. Javaloyes, *et al.*, Temporal localized Turing patterns in mode-locked semiconductor lasers, Optica **9**, 1386 (2022).

[9] P. Oswald, J. Baudry, and S. Pirkl, Static and dynamic properties of cholesteric fingers in electric field, Phys. Rep. **337**, 67 (2000).

[10] S. Echeverría-Alar and M. G. Clerc, Labyrinthine patterns transitions, Phys. Rev. Res. **2**, 042036 (2020).

[11] A. C. Newell and Y. Pomeau, Turbulent crystals in macroscopic systems, J. Phys. A: Math. Gen. **26**, L429 (1993).

[12] M. Le Berre, E. Ressayre, A. Tallet, Y. Pomeau, and L. Di Menza, Example of a chaotic crystal: The labyrinth, Phys. Rev. E **66**, 026203 (2002).

[13] Q. Ouyang and J.-M. Flesselles, Transition from spirals to defect turbulence driven by a convective instability, Nature (London) **379**, 143 (1996).

[14] S. J. Moon, M. D. Shattuck, C. Bizon, D. I. Goldman, J. B. Swift, and H. L. Swinney, Phase bubbles and spatiotemporal chaos in granular patterns, Phys. Rev. E **65**, 011301 (2001).

[15] S.-Q. Zhou and G. Ahlers, Spatiotemporal chaos in electroconvection of a homeotropically aligned nematic liquid crystal, Phys. Rev. E **74**, 046212 (2006).

[16] G. Xu, D. Vocke, D. Faccio, J. Garnier, T. Roger, S. Trillo, and A. Picozzi, From coherent shocklets to giant collective incoherent shock waves in nonlocal turbulent flows, Nat. Commun. **6**, 8131 (2015).

[17] M. G. Clerc and N. Verschueren, Quasiperiodicity route to spatiotemporal chaos in one-dimensional pattern-forming systems, Phys. Rev. E **88**, 052916 (2013).

[18] J. García-Ojalvo and J. Sancho, *Noise in Spatially Extended Systems* (Springer Science & Business Media, New York, 2012).

[19] G. Agez, M. G. Clerc, and E. Louvergneaux, Universal shape law of stochastic supercritical bifurcations: Theory and experiments, Phys. Rev. E **77**, 026218 (2008).

[20] E. Turitsyna, S. Smirnov, S. Sugavanam, N. Tarasov, X. Shu, S. Babin, E. Podivilov, D. Churkin, G. Falkovich, and S. Turitsyn, The laminar-turbulent transition in a fibre laser, Nat. Photon. **7**, 783 (2013).

[21] I. Roa González, B. Costa Lima, P. Pincheira, A. Brum, A. Macêdo, G. Vasconcelos, L. Menezes, E. P. Raposo, A. Gomes, and R. Kashyap, Turbulence hierarchy in a random fibre laser, Nat. Commun. **8**, 15731 (2017).

[22] P. J. Aguilera-Rojas, M. G. Clerc, S. Echeverría-Alar, Y. Soupart, and M. Tlidi, Fingerprint pattern bi-turbulence in a driven dissipative optical system, Chaos Solit. Fractals **182**, 114851 (2024).

[23] R. Alert, J. Casademunt, and J.-F. Joanny, Active turbulence, Annu. Rev. Condens. Matter Phys. **13**, 143 (2022).

[24] K. A. Takeuchi and M. Sano, Universal fluctuations of growing interfaces: Evidence in turbulent liquid crystals, Phys. Rev. Lett. **104**, 230601 (2010).

[25] Q. Ouyang and H. L. Swinney, Transition to chemical turbulence, Chaos **1**, 411 (1991).

[26] S. Ghashghaie, W. Breymann, J. Peinke, P. Talkner, and Y. Dodge, Turbulent cascades in foreign exchange markets, Nature (London) **381**, 767 (1996).

[27] E. A. L. Henn, J. A. Seman, G. Roati, K. M. F. Magalhães, and V. S. Bagnato, Emergence of turbulence in an oscillating Bose-Einstein condensate, Phys. Rev. Lett. **103**, 045301 (2009).

[28] A. Pikovsky and A. Politi, *Lyapunov Exponents: A Tool to Explore Complex Dynamics* (Cambridge University Press, Cambridge, 2016).

[29] C. Bandt and B. Pompe, Permutation entropy: A natural complexity measure for time series, Phys. Rev. Lett. **88**, 174102 (2002).

[30] I. Leyva, J. H. Martínez, C. Masoller, O. A. Rosso, and M. Zanin, 20 years of ordinal patterns: Perspectives and challenges, Europhys. Lett. **138**, 31001 (2022).

[31] H. Y. D. Sigaki, R. F. Souza, R. T. Souza, R. S. Zola, and H. V. Ribeiro, Estimating physical properties from liquid crystal textures via machine learning and complexity-entropy methods, Phys. Rev. E **99**, 013311 (2019).

[32] G. Tirabassi and C. Masoller, Entropy-based early detection of critical transitions in spatial vegetation fields, Proc. Natl. Acad. Sci. USA **120**, e2215667120 (2023).

[33] S. Y. Xiang, W. Pan, L. S. Yan, B. Luo, X. H. Zou, N. Jiang, and K. H. Wen, Quantifying chaotic unpredictability of vertical-cavity surface-emitting lasers with polarized optical feedback via permutation entropy, IEEE J. Sel. Top. Quantum Electron. **17**, 1212 (2011).

[34] L. Zunino, O. A. Rosso, and M. C. Soriano, Characterizing the hyperchaotic dynamics of a semiconductor laser subject to optical feedback via permutation entropy, IEEE J. Sel. Top. Quantum Electron. **17**, 1250 (2011).

[35] J. P. Toomey and D. M. Kane, Mapping the dynamic complexity of a semiconductor laser with optical feedback using permutation entropy, Opt. Express **22**, 1713 (2014).

[36] C. Quintero-Quiroz, S. Pigolotti, M. C. Torrent, and C. Masoller, Numerical and experimental study of the effects of noise on the permutation entropy, New J. Phys. **17**, 093002 (2015).

[37] L. J. Quintero-Rodríguez, I. E. Zaldívar-Huerta, Y. Hong, C. Masoller, and M. W. Lee, Permutation entropy analysis of the output of a laser diode under stimulated Brillouin scattering optical feedback, Opt. Express **29**, 26787 (2021).

[38] H. V. Ribeiro, L. Zunino, E. K. Lenzi, P. A. Santoro, and R. S. Mendes, Complexity-entropy causality plane as a complexity measure for two-dimensional patterns, PLoS One **7**, e40689 (2012).

[39] M. G. Clerc, A. Petrossian, and S. Residori, Bouncing localized structures in a liquid-crystal light-valve experiment, Phys. Rev. E **71**, 015205(R) (2005).

[40] S. Residori, Patterns, fronts and structures in a liquid-crystal-light-valve with optical feedback, Phys. Rep. **416**, 201 (2005).

[41] M. G. Clerc, T. Nagaya, A. Petrossian, S. Residori, and C. Riera, First-order Fréedericksz transition and front propagation in a liquid crystal light valve with feedback, Eur. Phys. J. D **28**, 435 (2004).

[42] P. J. Aguilera-Rojas, M. G. Clerc, and S. Navia, Optical feedback-induced spatiotemporal patterns with power law spectra in a liquid crystal light valve, Opt. Lett. **49**, 3292 (2024).

[43] M. G. Clerc, G. González-Cortés, V. Odent, and M. Wilson, Optical textures: Characterizing spatiotemporal chaos, Opt. Express **24**, 15478 (2016).

[44] A. J. Alvarez-Socorro, M. G. Clerc, G. González-Cortés, and M. Wilson, Nonvariational mechanism of front propagation: Theory and experiments, Phys. Rev. E **95**, 010202(R) (2017).

[45] R. Neubecker, G.-L. Oppo, B. Thuering, and T. Tschudi, Pattern formation in a liquid-crystal light valve with feedback, includ-

ing polarization, saturation, and internal threshold effects, Phys. Rev. A **52**, 791 (1995).

[46] G. Agez, C. Szwaj, E. Louvergneaux, and P. Glorieux, Noisy precursors in one-dimensional patterns, Phys. Rev. A **66**, 063805 (2002).

[47] See Supplemental Material at http://link.aps.org/supplemental/10.1103/rdhb-x2gv for Video 1 and Video 2 showing the evolution of the experimental and numerical pattern dynamics, respectively.

[48] R. N. Youngworth, B. B. Gallagher, and B. L. Stamper, An overview of power spectral density (PSD) calculations, Opt. Manuf. Test. VI **5869**, 206 (2005).

[49] G. Huyet, M. C. Martinoni, J. R. Tredicce, and S. Rica, Spatiotemporal dynamics of lasers with a large Fresnel number, Phys. Rev. Lett. **75**, 4027 (1995).

[50] C. Denz, M. Schwab, and C. Weilnau, *Transverse-Pattern Formation in Photorefractive Optics* (Springer, Berlin, 2003).

[51] T. Ackemann and W. Lange, Non- and nearly hexagonal patterns in sodium vapor generated by single-mirror feedback, Phys. Rev. A **50**, R4468(R) (1994).

[52] A. Wolf, J. B. Swift, H. L. Swinney, and J. A. Vastano, Determining Lyapunov exponents from a time series, Physica D **16**, 285 (1985).

[53] E. Ott, *Chaos in Dynamical Systems* (Cambridge University Press, Cambridge, 2002).

[54] A. C.-L. Chian, P. R. Munoz, and E. L. Rempel, Edge of chaos and genesis of turbulence, Phys. Rev. E **88**, 052910 (2013).

[55] Y.-C. Lai and T. Tél, *Transient Chaos: Complex Dynamics on Finite Time Scales* (Springer Science & Business Media, New York, 2011), Vol. 173.

[56] M. G. Clerc, S. Residori, and C. S. Riera, First-order Fréedericksz transition in the presence of light-driven feedback in nematic liquid crystals, Phys. Rev. E **63**, 060701(R) (2001).